Award Accounts
The Chemical Society of Japan Award for Young Chemists for 2005

Functionalities of a Nanoporous Crystal $12CaO\cdot7Al_2O_3$ Originating from the Incorporation of Active Anions

Katsuro Hayashi,* Masahiro Hirano, and Hideo Hosono

Materials and Structures Laboratory and Frontier Collaborative Research Center,
Tokyo Institute of Technology, R3-34, 4259 Nagatsuta, Yokohama 226-8503

Received September 6, 2006; E-mail: k-hayashi@lucid.msl.titech.ac.jp

A cage structure formed in a positively charged lattice framework of $12CaO\cdot7Al_2O_3$ (C12A7) is utilized to incorporate and release chemically unstable anions, imparting chemical and electronic activities to this material. High concentrations of oxygen radical anions, i.e. O^- and $O_2{}^-$, are formed efficiently in these cages under a high oxygen activity condition. The O^- ion, which is the strongest oxidant among all the reactive oxygen species, can be extracted from the cages into an external vacuum by applying an electric field with thermal assistance. In contrast, hydrogen-reduction processes allow the formation of hydride (H^-) ions in the cage. H^- ion-incorporated C12A7 exhibits a persistent insulator–conductor conversion upon irradiation with ultraviolet-light or electron-beam. The irradiation-induced conversion mechanism and electronic transport characteristics are discussed on the basis of experimental evidence and first-principle theoretical calculations. Electrons released from the H^- ions are trapped by the cages and subsequent inter-cage hopping of the electrons is responsible for the electrical conduction. Furthermore, a severe reducing environment enables us to substitute electrons almost completely for anions in the cages, forming a stable inorganic electride. Finally, the formation of these active anions in this material is examined in terms of electronic structures, thermodynamics, and structural features of the cage.

1. Introduction

$12CaO\cdot7Al_2O_3$ (C12A7) is commonly known as a natural mineral "mayenite" as well as a constituent of calcium aluminate cements produced and consumed on a large-scale.[1] Although C12A7 appears to be useful only for structural material purposes, it has huge potential for exhibiting active functionalities, if its unique nanostructure embedded in the lattice is fully utilized. Its crystal structure, as illustrated in Fig. 1, was determined in the early '70s.[2] An incomplete network of AlO_4 tetrahedra incorporated with Ca ions forms a cage structure. The unit cell is composed of two formula units ($Z = 2$) and is convenient to be expressed as $[Ca_{24}Al_{28}O_{64}]^{4+} + 2O^{2-}$. The $[Ca_{24}Al_{28}O_{64}]^{4+}$ component denotes the lattice framework containing 12 cages. Each cage has an inner free space of $\approx$0.4 nm in diameter, approximately S_4 symmetry along the axis passing through two Ca ions and the center of the cage, and is connected to its eight nearest neighbors via a Ca–O–Ca–Al–O–Al ring. Only a mean effective charge of $+1/3|e|$ ($=+4|e|/12$ cages, where e is the elemental charge) is assigned to each cage. The remaining two O^{2-} ions do not belong to the framework, but randomly occupy 1/6 of the inner cage sites, thereby are referred to as "free oxygen" or "extra-framework oxide ions." The presence of extra-framework O^{2-} ions is most likely an origin of the fast oxide ion conduction

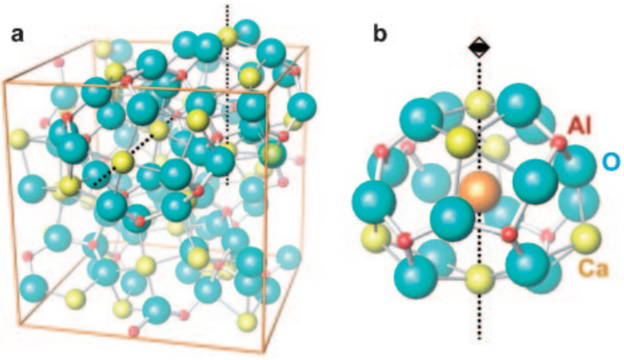

Fig. 1. Crystal structure of C12A7. Each atom is described with 50% of the actual ion size. (a) Lattice framework with the space group $I\bar{4}3d$ and the lattice constant $\approx$1.2 nm. Highlighted part is complete two neighboring cages, where some of atoms extend outside the unit cell. Extra-framework anions are omitted in this figure for simplicity. The S_4 axes, indicated by dashed lines, are directed to $\langle 100\rangle$, which of neighboring cages are perpendicular to each other. (b) Single cage incorporating an extra-framework anion at the cage center. The S_4 symmetry of each cage is preserved only approximately because the cages are distorted by extra-framework ions.

Published on the web May 14, 2007; doi:10.1246/bcsj.80.872

observed in a dry oxidative atmosphere.[3] Furthermore, the O^{2-} ions can be partially or completely replaced by various anions such as OH^-,[4] F^-, and Cl^-.[5] Monovalent anions occupy 1/3 of the total cage site at the maximum, which corresponds to an anion concentration of $2.3 \times 10^{21}\,cm^{-3}$. Since OH^-, F^-, and Cl^- ions are rather chemically stable, conventional C12A7 have never offered any chemical and electronic active properties. Such anion-exchange properties are complementary to those of conventional nanoporous crystals, e.g. zeolites, whose lattice framework is negatively charged and formed with extra-framework cations.

Our approach to render C12A7 an active material involves the incorporation of chemically unstable, i.e. "active," anionic species into the positively charged cage by suitable chemical processes. One important achievement of this approach is a formation of highly reactive oxygen radical anions, O^- and $O_2{}^-$, inside cages with extraordinarily high concentrations. Thermal annealing in oxygen atmospheres can almost completely replace the extra-framework oxide ions with these radical anions. Their formation process, thermodynamics, and an extraction to vacuum as an O^--ion beam are described in Section **3**. Heat-treatments in hydrogen atmospheres form another kind of reactive anion, hydride (H^-) ions, in the cages. H^--incorporation affords light- or electron-beam-induced insulator–conductor conversions. Mechanisms of the irradiation-induced carrier formation and the resultant electrical conduction are discussed in Section **4**. Section **5** describes the "C12A7 electride," where electrons are substituted for the extra-framework anions, thereby occupying the free space of the cages behaving like anions. In this article, the electrons trapped in the cage are also treated as an active anions species. Section **6** discusses some aspects of the active anion formation to elucidate origins of their stable formation from thermodynamic and quantum mechanical points of views. Finally, concluding remarks are given in Section **7**. Before describing our approach to the active anion incorporation, we begin with syntheses of various forms of C12A7, which are the key of our study for exploring novel functionalities in this material.

2. Synthesis of Various Forms of C12A7

Fabrication processes of translucent ceramics, single crystal and thin films are described in this section. It is noted that several properties specific to C12A7 sometimes help and sometimes hinder these processes.

Sinterability of C12A7 has been considered to be poor. However, a fully densified translucent C12A7 ceramics was fabricated by the sintering of a green body made of hydrated C12A7 powder (Fig. 2a) in a dry oxygen atmosphere.[6] The dry atmosphere enhances densification much better than a wet atmosphere. The visible light transmittance for the ceramic plate with a thickness of 1 mm was improved up to ≈70% by sintering at 1300 °C for 48 h (Fig. 2b). The improvement is likely ascribed to efficient annihilation of pores at the grain boundaries, whose light-scattering principally deteriorates the transparency of ceramics. Since C12A7 has a high solubility of water owing to the formation of extra-framework OH^- ions and oxygen gas as oxygen radical anions (The detail will be described in the next section.), residual water and/or oxygen molecules existing in pores at the initial stage of the sintering process successively dissolve into the lattice as the densification proceeds. As a result, these pores shrink and are eventually annihilated.

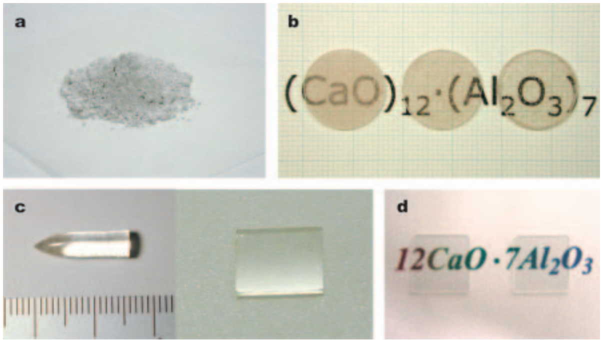

Fig. 2. Photographs of various forms of C12A7. (a) Powders synthesized by a conventional solid-state reaction. (b) Translucent ceramics obtained by sintering at 1300 °C for 12 (left), 24 (center), and 48 h (right) in dry oxygen atmosphere.[6] (c) FZ-grown single crystals. Left is a tail part of the grown ingot and right is a polished single-crystal plate sliced from the ingot. (d) Thin film deposited on MgO substrate.

Single crystal growth of C12A7 has been examined in oxygen-containing atmospheres, because C12A7 decomposes into a eutectic of $CaAl_2O_4$ (CA) and $Ca_3Al_2O_6$ (C_3A) in an inert atmosphere at high temperature.[7] Whatmore et al. have grown single crystals with ≈20 mm in diameter by the Czochralski (CZ) method using Ir crucible.[8] However, Ir-inclusion caused a strong Tyndal scattering, and hence the crystal is not adequate for evaluating optical properties.

Watauchi et al.[9] have grown a colorless transparent C12A7 crystal with ≈5 mm in diameter by the floating zone (FZ) method (Fig. 2c). A conventional FZ technique is very difficult to apply to C12A7 crystal growth, because C12A7 melt is a good solvent for oxygen gas,[10] whose precipitation upon the crystallization enhances the formation of oxygen bubbles or pores. Furthermore, C12A7 has a good light-transmission in infrared–visible range and a low thermal conductivity, making it difficult to form an appropriate solid–liquid interface for eliminating bubbles from a growing crystal by the lamp heating. These problems have been solved by reducing the growth rate to $1\,mm\,h^{-1}$ and incorporating an alumina tube into the heating zone to improve the temperature uniformity. FZ-grown crystals were exclusively used for the experiments described in this article.

Recently, Kurashige et al. have optimized conditions of the CZ-growth by employing the radio frequency induction heating of Ir-crucible in a diluted oxygen atmosphere, and obtained inclusion-free high-quality crystals with an ingot diameter of more than 25 mm. However, the crystals are colored orange by the incorporation of Ir^{4+} ions from the crucible with a concentration of $\approx 5 \times 10^{17}\,cm^{-3}$.[11]

Polycrystalline C12A7 thin films (Fig. 2d) have been prepared by a room-temperature deposition of amorphous C12A7 films on MgO substrates using a pulsed laser deposition (PLD) method followed by a thermal annealing at temperatures above ≈900 °C,[12,13] which corresponds to the onset temperature of the crystallization of C12A7 glasses.[14] Below this temperature, neither the post annealing nor physical deposition on a heated

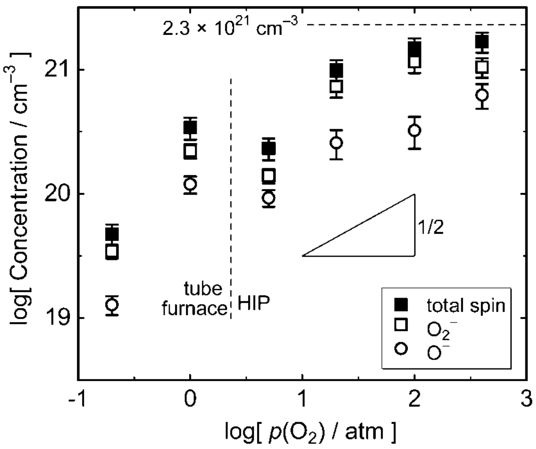

Fig. 3. Dependence of the oxygen radical concentration on the oxygen partial pressure during heat-treatment in C12A7. Polycrystalline sinters with 80% of theoretical density were heated up to 1350 °C and cooled with a rate of 200 $K\,h^{-1}$ in an atmospheric pressure tube furnace and a hot isostatic pressing (HIP) furnace.[19]

substrate results in the formation of a crystalline phase. Direct physical deposition of the crystalline film is possible only when the substrate temperature is much higher than ≈900 °C.

3. Active Oxygen Anions

3.1 Formation in Cages. Oxygen molecules adsorbed on metal oxides are converted to anionic oxygen radicals such as O_2^- and O^- when reduced by surface defects. They play a crucial role in an oxidation reaction on metal oxides.[15] Among the oxygen radicals, the reactivity of the O^- radical is exceptional. For example, O^- radical formed on a MgO surface reacts with hydrocarbons even below ≈90 K.[16] However, O^- formation methods so far developed, including an energetic light-irradiation and an adsorption of N_2O molecule on the surface, are not commensurate with their high costs from an industrial point of view. Nevertheless, chemists have been fascinated by the potential of the O^- radical for oxidation reactions at low temperature.

Hosono and Abe detected O_2^- radicals with a concentration of 1×10^{19} cm^{-3} in C12A7 synthesized in ambient air using an electron paramagnetic spin resonance (EPR).[17] Then, we found extremely high concentrations (in the order of 10^{20} cm^{-3}) of O^- as well as O_2^- formed in C12A7 with ≈80% of the theoretical density when heated in a dry oxygen atmosphere.[18] To the best of our knowledge, such a high concentration, corresponding to ≈10 atm in gas phase, has not been obtained in any other solids. Furthermore, the effect of oxygen partial pressure, $p(O_2)$, on the enhancement of the active oxygen radical formation was examined using a hot isostatic-pressing furnace (Fig. 3).[19] The total radical concentration of 1.7×10^{21} cm^{-3} was obtained for an $p(O_2)$ of 400 atm, which is close to the theoretical maximum concentration of monovalent anions in the cages as obtained from the total charge of the framework, 2.3×10^{21} cm^{-3}. This fact suggests that these radicals are incorporated in the cages.

The formation of oxygen radicals was markedly reduced with an increase in the water vapor pressure due to the formation of OH^- ions in the cages via the reaction, which hampers the incorporation of the oxygen radicals:[20]

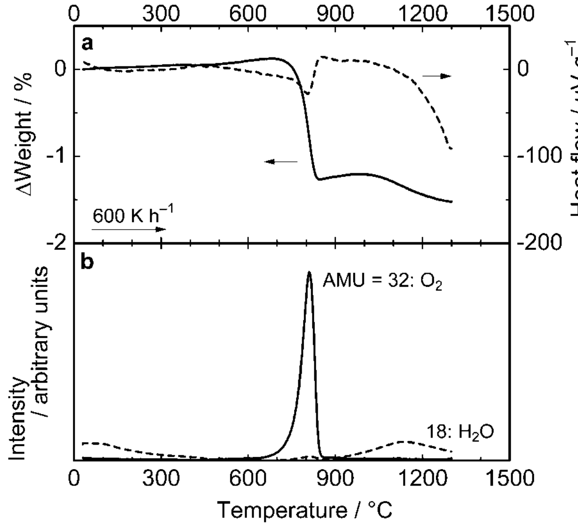

Fig. 4. Thermogravimetric-evolved gas combined analyses (TG-EGA) of C12A7 polycrystalline ceramics with the theoretical density of ≈80%. The samples were preheated at 550 °C for 36 h in a dry O_2. Thermogravimetric-differential thermal analyses (a) and mass spectroscopy (b) were carried out during heating with a rate of 600 $K\,h^{-1}$ in a He carrier gas flow.[23]

$$O^{2-}(c) + \mathrm{null}(c) + H_2O(g) \rightarrow 2OH^-(c), \qquad (1)$$

where (c) and (g) specify the species in the cage and the gas phase, respectively, and null denotes the empty cage. The formation of oxygen radicals in a dry oxygen atmosphere is attributed to the absorption of oxygen molecules into C12A7, where the dominant reaction is most likely:

$$O^{2-}(c) + O_2(g) \rightarrow O^-(c) + O_2^-(c). \qquad (2)$$

Absorption of O_2 gas to form O_2^- radical was evidenced by detection of $^{17}O_2^-$ radicals by the EPR after annealing in $^{17}O_2$.[21] From the EPR study, the geometry of O_2^- in a cage with respect to the cage wall and its temperature-dependent dynamic motion inside the cage were also determined. Equation 2 also indicates that the formation of oxygen radicals causes an oxygen excess state with respect to the stoichiometric composition of C12A7. Indeed, as observed in Fig. 4, the excess oxygen desorbs when heated to ≈700 °C in an inert gas atmosphere.[22,23] The weight loss reasonably agreed with the amount of oxygen radicals evaluated from the EPR intensities, further supporting the radical formation process represented by Eq. 2. However, observed weight loss slightly exceeds the amount of oxygen radicals. The discrepancy is ascribed to the formation of O_2^{2-} ions in the cages. Although diamagnetic O_2^{2-} ion is not detectable by the EPR, its presence was suggested from an enhanced Raman band at ≈730 cm^{-1}.[15] Estimated concentration of O_2^{2-} ions formed in dry oxygen atmosphere was in the range of $10^{18\text{–}20}$ cm^{-3}.

During the oxygen absorption process, O^- and O_2^- ions formed at the surface diffuse inward, while an equivalent amount of O^{2-} ions diffuse outward. As a result, oxygen radicals accumulate inside the bulk. Theoretical calculations on the diffusion show that the direct inter-cage migration of the

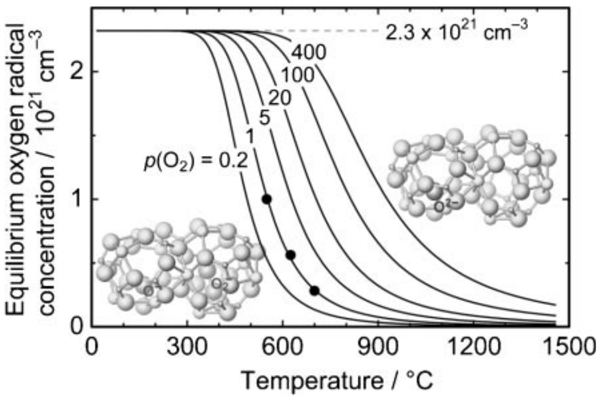

Fig. 5. Temperature dependence of oxygen radical concentration at equilibrium for several oxygen partial pressures. Circles denote measured equilibrium concentrations and solid lines are thermodynamically calculated ones.[25]

extra-framework oxygen species through the opening of the cages is not feasible, instead they diffuse by exchanging with the framework O^{2-} ions.[24] This fact suggests that extra-framework O^- and $O_2{}^-$ ions are involved in equilibrium reactions with framework O^{2-} ions. Although it is impossible to assess every possible reactions, a simplification of all possible reactions into Eq. 2 makes it possible to evaluate thermodynamically the formation of oxygen radicals from oxygen gas absorption. Figure 5 shows the measured and thermodynamically assessed equilibrium total concentration of oxygen radicals. This plot enables us to predict temperature and $p(O_2)$ dependences of the equilibrium oxygen radical content.[25] The estimated enthalpy change for Eq. 2 was $-131\,\mathrm{kJ\,mol^{-1}}$ ($-1.4\,\mathrm{eV}$). Exothermic reaction indicates that the equilibrium concentrations of oxygen radicals are enhanced with decreasing temperature. Results of thermodynamic assessment in Fig. 5 predict that the total concentration reaches the maximum concentration below ≈300 °C. However, since a decrease in temperature suppresses the bulk diffusion rate of oxygen species, the rate of the oxygen radical formation is also limited by the diffusion rate of the oxygen radicals.[25] Thus, it is practically impossible to obtain the maximum concentration by such low-temperature treatment. For example, it takes more than 100 h to obtain concentrations higher than $2 \times 10^{21}\,\mathrm{cm^{-3}}$ in fine powders with a diameter of 1 µm at 400 °C under $p(O_2) = 1$ atm. Practical temperatures for the thermal treatment under atmospheric pressure are in the range of ≈600–800 °C.[26] On the other hand, equilibrium concentrations at higher temperatures are proportional to the square root of $p(O_2)$. This dependence agrees with those observed for the high pressure oxygen treatment (See Fig. 3).

3.2 Generation of O^- Ion Beam. Generation of O^- ions in a vacuum has been a focus for the surface oxidation or modification of materials. However, ion sources that can selectively generate O^- ions have not come into general use in the industry. So far, the most promising O^- ion source under the development is a plasma-sputter-type source.[27] The principle of this device is the generation of negative ions by the conversion of plasma-generated neutral or positive particles on an electrode whose work function is lowered by Cs deposition. Although some practical devices, which generate O^- ion current on the order of milliamperes by a few hundred watt power supply, have been developed, the necessity of continuous supply of Cs limits its applications.

Torimoto et al. have proposed a novel negative ion generation method that has totally different principle from conventional methods.[28] They inserted a tubular yttrium-stabilized zirconia (YSZ) with porous gold electrodes on both surfaces of the tube into a vacuum chamber. In addition, an extraction electrode was proximately placed 15 mm away from the outside of the tube. They observed an O^- emission current on the order of nano-amperes with an extraction bias of several hundred volts applied between the inside electrode and the extraction electrode while heating of the tube at ≈700 °C with a supply of oxygen gas inside the tube. They considered that O^{2-} ions conducted through the YSZ at elevated temperature are emitted as O^- ions with an equivalent amount of electron emission.[29] Direct emission of negative ion from solids is a promising method for realizing a Cs-free O^- negative ion source, although a current on the order of nanoamperes is still insufficient for the practical use.

Since C12A7 is also an oxide ion conductor, and moreover can accommodate the O^- ion in its cages, this material seems to be a better candidate for the direct O^- ion emission from a solid. A C12A7 ceramic disc containing a large amount of O^- ($1 \times 10^{20}\,\mathrm{cm^{-3}}$) and $O_2{}^-$ ($3 \times 10^{20}\,\mathrm{cm^{-3}}$), was prepared and then a dc voltage was applied between anode formed on the backside of the disc and an extraction electrode placed at ≈10 mm away from the front surface of the disk in a vacuum chamber. Nearly pure O^- ion emission from the surface was confirmed by mass spectroscopy.[30–33] This result is in clear contrast from the YSZ, which emits equimolar O^- ions and electrons. When the sample was heated to ≈800 °C and the applied field was increased to $\approx 1\,\mathrm{kV\,cm^{-1}}$, the O^- current density exceeded $\approx 1\,\mathrm{\mu A\,cm^{-2}}$, which is three orders of magnitude higher than that obtained in the YSZ emitter. The O^- ion current was sustained until the oxygen radicals inside the C12A7 were completely consumed. In addition, it is noted that O^- ions can be extracted from a bare surface of C12A7, while the YSZ emitter requires porous gold coatings, which may catalyze the dissociation of O^{2-} ions into a pair of O^- ion and an electron.[29]

At first glance, efficient O^- ion emission from C12A7 is likely ascribed to the direct extraction of O^- ions from the cages near the surface. However, as suggested by the theoretical study on the transport of oxygen species,[24] the direct inter-cage migration of O^- is not feasible. Thus, the direct emission from the surface cage also seems to be not allowed. Here we point out that intense O^- emission occurs in the similar temperature range of the spontaneous oxygen gas desorption as observed in Fig. 4b. Recently, we observed that O_2 gas effused from an oxygen radical-incorporated C12A7 into vacuum in a similar temperature range irrespective of the application of the extraction field.[34] Such an oxygen desorption is caused by the relaxation of a non-equilibrium oxygen-excess state to the equilibrium near-stoichiometric state. We speculate that the O^- ion emission from C12A7 is promoted by this driving force, and then O^- ions are efficiently formed on the surface during the oxygen desorption process. In addition, the following properties of C12A7 likely accommodate the supply of the O^- ion

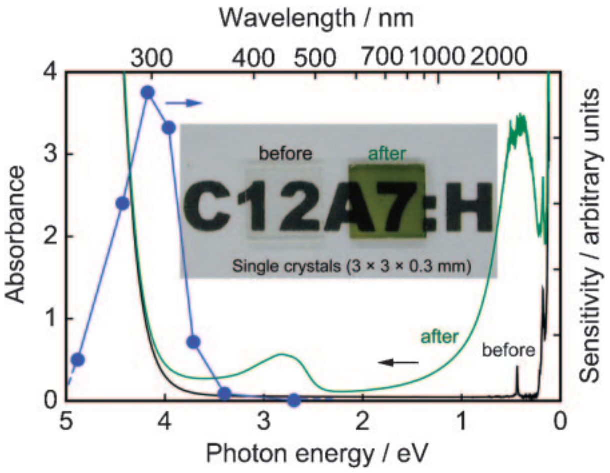

Fig. 6. Optical absorption spectra for C12A7:H$^-$ single crystals before (black line) and after (green line) illumination with UV light. Blue filled circles denote the photon energy dependence of the sensitivity on the coloration. Inset is a photograph of single crystals before and after the illumination.[35]

to be emitted to vacuum without surplus electron formation. Various oxidation states (O_2^-, O_2^{2-}, O^-, and O^{2-}, in the lower to higher order) are allowed for the extra-framework oxygen anions, and inter-cage electron transfer is fast, as described in the next section. Excess electrons, even if they are generated, are easily accommodated by the valence change of the extra-framework oxygen anions before being emitted to the vacuum.

In summary, C12A7 appears to have suitable properties for the efficient O^- emission to vacuum. However, continuous generation of high-density ion beam likely requires a supply of oxygen from backside of the C12A7 membrane to maintain an oxygen-excess state. Development of a practical ion source depends on solution of these technical problems.

4. Incorporation of H$^-$ Ions

4.1 Photoinduced Conversion of C12A7:H$^-$ from Insulator to Conductor. Electronic conduction in light metal oxides was first found in C12A7, in which hydride ion (H$^-$) was incorporated into the cages by thermal treatment in a hydrogen atmosphere.[35] The as-prepared H$^-$-incorporated C12A7 (C12A7:H$^-$) was colorless and a good insulator with an electronic conductivity of less than 10^{-10} S cm^{-1}. However, upon illumination with UV light around 300 nm, the C12A7:H$^-$ became yellowish green due to photo-absorption by 2.8 and 0.4 eV bands (Fig. 6), accompanied by an increase in the conductivity by more than 10^{10} times. Around room temperature, the conductive state had an electrical conductivity of $\approx$0.1–10 S cm^{-1} with a mobility of $\approx$0.1 cm^2 s^{-1} V^{-1}. The conductivity increased with temperature with an activation energy of $\approx$0.1 eV. The optical absorption and the conductivity never decay at room temperature even after the irradiation was stopped. However, when heated above $\approx$300 °C, C12A7:H$^-$ reverted back to being an insulator, and the optical absorption intensities decayed concomitantly. Further heating above $\approx$550 °C caused the release of H_2 gas and a simultaneous loss of photosensitivity. Upon illumination with UV light at room temperature, H$^-$ ion is photolyzed to release an electron, which is then trapped in a cage, and the inter-cage migration of the electron is responsible for the electrical conduction. The detail of this process will be discussed later.

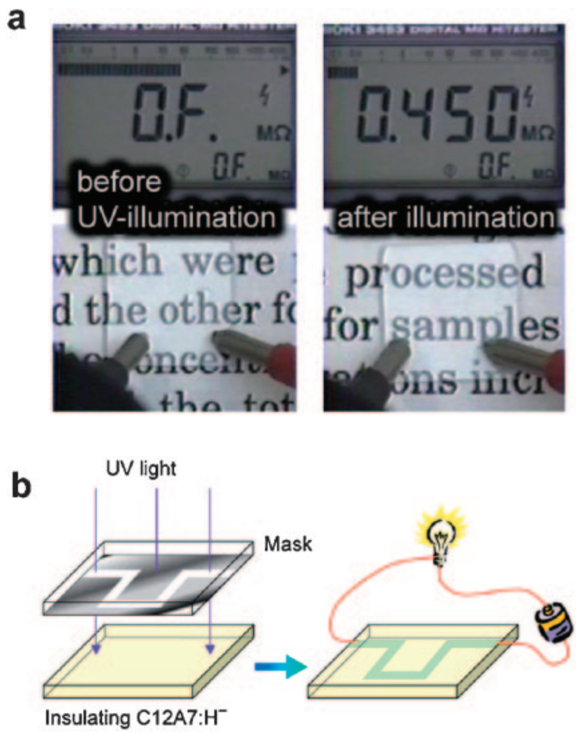

Fig. 7. Photoinduced insulator–conductor conversion in C12A7:H$^-$ thin films. (a) Both electrically insulating (lower left) and conductive (lower right) films appear colorless and transparent. (b) Schematic of a direct patterning of a conductive pattern by the UV-illumination through a patterned mask.

The insulator–conductor conversion by UV-illumination was also possible in C12A7:H$^-$ thin films, in which H$^-$ ions were formed either by thermal treatment in a hydrogen atmosphere at 1200 °C[12] or via the hot ion implantation of H$^+$ ions into the films.[13] The visible light absorption loss was estimated to be only 1% for 200 nm-thick films with an electrical conductivity of 1 S cm^{-1} at room temperature. Thus, the conductive film was also colorless and transparent (Fig. 7a). These properties enable novel applications such as a direct optical patterning of transparent electronic circuits on the insulating media (Fig. 7b).

The generation of persistent carrier electrons in C12A7:H$^-$ by an electron-beam (EB) irradiation was also examined.[36] The EB irradiation to an insulating C12A7:H$^-$ single crystal afforded an electrical conductivity to the surface layer of the crystal and a green coloration identical to that induced by the UV-light illumination. The carrier electron formation was saturated at an EB dose of 300 μC cm^{-2}, which is comparable to the sensitivity of conventional photoresists for the EB lithography. The yield per incident electron for the carrier electron generation in C12A7:H$^-$ was estimated to be as high as 30 for an acceleration voltage of 25 keV. Such a high sensitivity makes it possible to form a fine conductive patterning directly on the surface of the C12A7:H$^-$ using a conventional EB-exposure system without a photomask and an EB-resist.

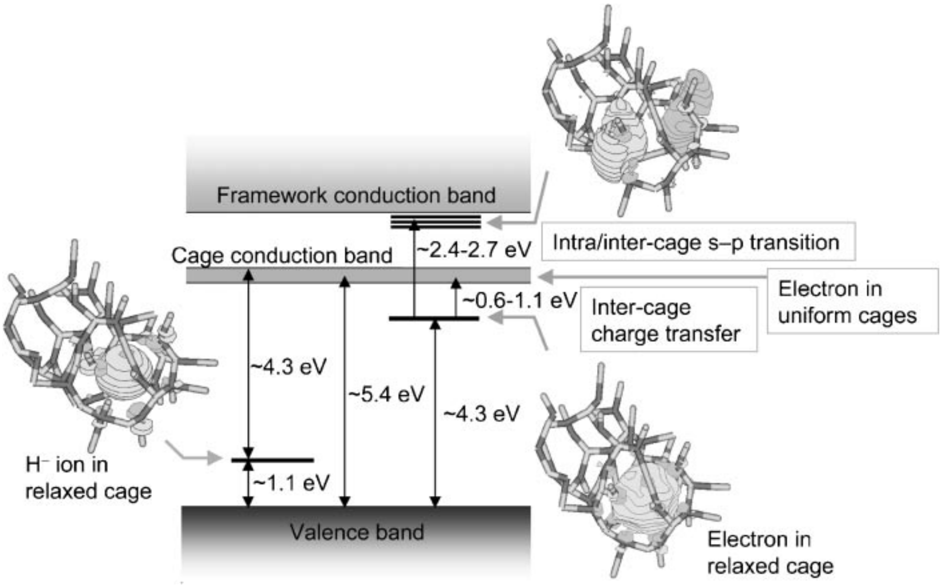

Fig. 8. A schematic of the energy levels in C12A7 incorporating either H^- ions or electrons, together with the corresponding wave functions obtained by first-principle calculations based on the embedded cluster approach. The excitation from the localized electronic state (F^+-like center) to the cage conduction band (≈0.6–1.1 eV) corresponds to the inter-cage charge-transfer transition. Excitations to the higher energy (2.4–2.7 eV) levels correspond to the s–p transitions.

This technique may provide an opportunity for investigating mesoscopic electronic properties of this material.

4.2 Mechanism of the Photoinduced Conversion. Sushko et al. have performed a theoretical calculation based on the density functional theory and the embedded cluster approach, which fully account for the lattice relaxation around a defect,[37–39] to clarify electronic states of H^- or electron in cages (F^+-like center) and mechanism of the irradiation-induced insulator–conductor conversion. Results of the calculation are summarized in Fig. 8. The H^- ion occupies the center of a cage and is stabilized by a strong inward relaxation of the cage, so that two Ca ions on the S_4 axis are displaced towards the H^- and the Ca–Ca distance decreases from 5.6 Å in the empty cage to 5.0 Å in the presence of H^-. Energy level of the H^- ion is located ≈1.1 eV above the valence band maximum (VBM), and the two electrons occupying this level are localized well within the cage. The empty cage states forms a narrow conduction band, called a "cage conduction band (CCB)," which is located ≈5.4 eV above VBM and ≈2 eV below the framework conduction band minimum (FCBM). When an electron is incorporated into a cage, its energy level is lowered by ≈1 eV from CCB minimum due to strong lattice relaxation similar to the H^- incorporation. As a result, the electron becomes localized in the cage in the same manner as an electron is localized in an anion vacancy in alkali halides (F centers) or alkaline-earth oxides (F^+ centers). Such an electron center in C12A7 is, therefore, termed an "F^+-like center." Since each cage is connected directly to several other cages, electrons are able to hop to neighboring cages with activation energy of only ≈0.1 eV, inducing a polaronic electrical conductivity. Experimentally observed activation energy agrees with that obtained by the theoretical evaluation. In addition, the F^+-like center induces two absorption bands with peaks at ≈0.4 and ≈2.8 eV (See Fig. 6). These bands are assigned to the inter-cage charge-transfer and the intra- or inter-cage s–p transitions of the electron, respectively.

The theoretical calculations confirm that the insulator–conductor conversion is induced by the photoionization of the H^- ion to form a pair of H^0 atom and an electron under excitation of ≈4.3 eV:[40]

$$H^-(c) + \mathrm{null}(c) \rightarrow H^0(c) + e^-(c). \quad (3)$$

These theoretical analyses are consistent with experimentally observed formation of electrons by UV-light with the efficiency maximum at ≈4.1 eV. However, EPR measurement of conductive C12A7:H^- after the UV-illumination at room temperature detected only a signal of the F^+-like center. H^0 was never detected at room temperature.[35]

The simultaneous formation of both species was only verified by the UV-illumination at low temperatures. Figure 9a shows an EPR spectrum after the illumination at 4 K, revealing that nearly equal amounts of H^0 atom and F^+-like centers were generated.[41] This result supports the presence of H^- ions and its photo-dissociation reaction. Furthermore, the H^0 concentration was found to decrease abruptly with increasing temperature and disappeared completely above ≈100 K, while the F^+-like centers survived above room temperature (Fig. 9b). This result is only explained by a conversion of a part of the H^0 atoms into diamagnetic H^+ ions above ≈100 K.

The H^0 atom is expected to be so unstable that it may further decompose into an H^+ ion and an electron. As such, these H^+ ions may form O–H bonds with framework O^{2-} ions. However, the theoretical calculations suggest that a pair of H^+ ion and electron existing in a same cage is energetically not advantageous as compared to the single H^0 atom in the cage.[42] If the H^+ ions diffuse along other framework O^{2-} ions to be trapped by extra-framework O^{2-} ions, they may be stabilized as extra-framework OH^- ions. These processes are described as:

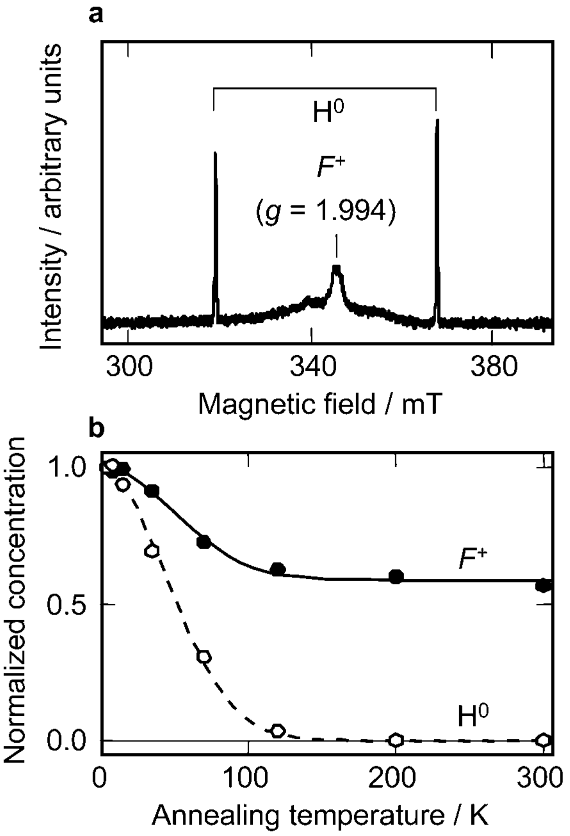

Fig. 9. EPR of C12A7:H^- measured at 4 K. (a) X-band dispersion mode spectra of C12A7:H^- irradiated with the UV-light at 4 K, showing a hyperfine doublet structure due to an H^0 and a broad singlet band due to the F^+-like center. **b**. Decay of H^0 and F^+-like centers by isochronal annealing each for 15 min. H^0 was completely annihilated above ≈200 K, while ≈60% of the F^+ centers remain even at 300 K.[41]

$$H^0(c) + O^{2-}(c) \rightarrow e^-(c) + OH^-(c). \quad (4)$$

The summation of Eqs. 3 and 4 gives a reaction that generates two electrons from a single H^- ion:

$$H^-(c) + \text{null}(c) + O^{2-}(c) \rightleftharpoons 2e^-(c) + OH^-(c). \quad (5)$$

This process is consistent with the absence of H^0 atoms at >100 K, and hence the most feasible candidate for persistence of the irradiation-induced electron generation process.

This reaction was validated by an experimental study of the high-temperature electrical conductivity of C12A7:H^- combined with a theoretical analysis.[43] We observed that C12A7:H^- without the UV-illumination had an electrical conductivity about 1–2 orders of magnitude larger than that expected from the oxide ion conductivity in a temperature range ≈550–300 °C, in which C12A7 retains H^- ions stably (Fig. 10a). Since the conductivity increases with the H^- concentration, apparently possible carriers are electrons thermally dissociated from H^- ions. The apparent activation energy for the electron generation was ≈0.7 eV, while the theoretical calculation[42] gave an estimate of the energy cost for the thermal dissociation of H^- as ≈3.5 eV (Fig. 10b), which is much larger than the observed activation energy. However, if H^0 further decomposes to form an OH^- ion and an electron, this process has an energy gain of ≈2.5 eV. Consequently, the energy difference between the initial and final states in Eq. 5 is decreased to ≈1.0 eV. If the experimentally observed activation energy (≈0.7 eV) is interpreted according to this process, double of the apparent activation energy (+1.4 eV) corresponds to the enthalpy change for this reaction. This value reasonably agrees with the theoretically estimated energy difference ≈1.0 eV. The equilibrium reaction of Eq. 5, therefore, provides a sound explanation for the thermal generation of the carrier electrons in the medium temperature range 550–300 °C.

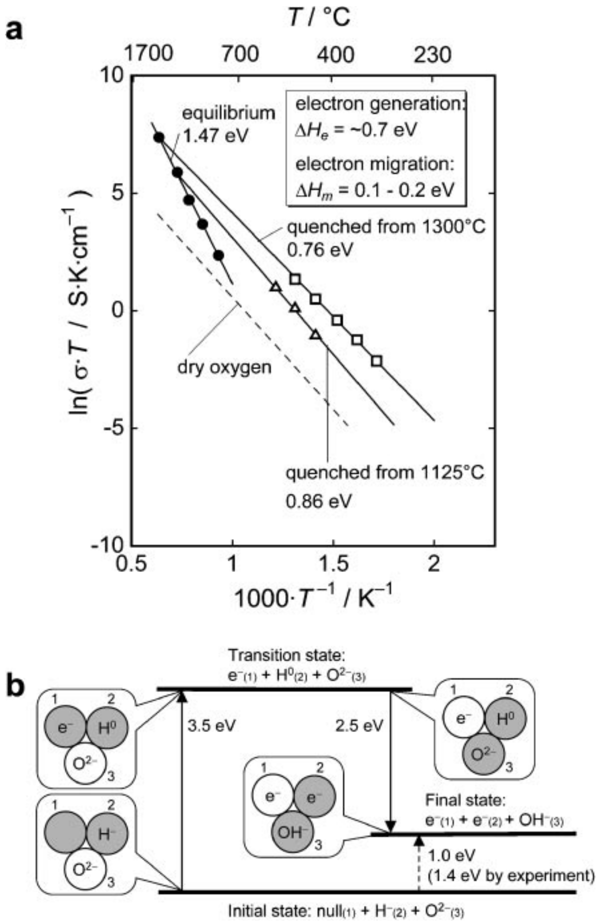

Fig. 10. Generation of electron carrier by thermal activation in C12A7:H^- (a) Electrical conductivity of C12A7 in equilibrium with 0.2 atm H_2 (filled circles with solid line) and of quenched C12A7 (open squares and triangles with solid lines). Dashed line indicates the oxide ion conductivity measured in a dry oxygen atmosphere. (b) Assessment of the energy change associated with the internal equilibrium using theoretical calculations. The illustrations schematically show the cage and extra-framework species. The calculations are performed for configurations composed of two shaded cages in each energy level.[43]

The conductive state of C12A7:H^- resulting from the photo-irradiation is also ascribed to the generation of two-electrons and H^+ ion from an H^- ion, which is completed by OH^- ion formation. According to the scheme in Fig. 10b, the persistence of the photo-induced conductive state is due to the presence of a high potential barrier for the reverse reaction. The barrier height (2.5 eV) arises mainly from strong O–H bond in the extra-framework OH^- ion.[42] Thus, the persistence of the conductive state is ascribed to the stability of the OH^- ion. It is also noted that the photo-induced conversion necessitates the presence of O^{2-} ions as well as H^- ions in the cages.

5. C12A7 as an Electride

Electrides are special crystalline compounds, in which electrons are confined in their crystalline cavities or channels, serving as anions. In traditional electrides, cations correspond to alkali ion-clathrates with cage structures constructed by organic complexants.[44] Owing to such a unique structure, electrides have unique properties for potential applications, such as reducing agents in chemical synthesis and electron emitter with a low work function. Unfortunately, these organic electrides degrade at room temperature or in ambient air. Thus, the study of the electrides has been focused on those having inorganic lattice framework to achieve proper stabilities. One example is a zeolite ITQ-4 intercalated with cesium.[45] Although this inorganic electride is stable at room temperature, it is still not durable in ambient air. In a broad sense, conductive C12A7 is regarded as an inorganic electride, where electrons are well confined to the free space of a cage. The conductive C12A7 is only an electride that is stable above room temperature in ambient air. However, the maximum electron concentration obtained by the hydrogen-reduction and subsequent UV-irradiation process is $\approx 1 \times 10^{20}\,cm^{-3}$, which is only a few tenths of the theoretical maximum concentration. When all the extra-framework anions are eliminated from the cages, only electrons occupy their inner space, and then such C12A7 is regarded as an electride in a more strict sense.

Matsuishi et al. have examined enhancement of the electron concentration by chemical reduction using Ca metal,[46] which has the highest oxide formation enthalpy among all elements. C12A7 single crystals were encapsulated with calcium metal shots in an evacuated silica glass ampoules, then they were annealed at 700 °C for 4–240 h. The extra-framework O^{2-} ions were selectively removed from crystals by forming CaO layers on the surfaces via reaction:

$$O^{2-}(c) + null(c) + Ca(s) \rightarrow 2e^-(c) + CaO(s), \qquad (6)$$

where (s) denotes the solid phase. Figure 11 shows changes in the appearance of single crystals with annealing time and their temperature dependences of electrical conductivity. Accompanying a change in the coloration over the treatment time, the electrical conductivity at room temperature increased up to $\approx 100\,S\,cm^{-1}$. The electron concentration was on the order of $10^{21}\,cm^{-3}$ when the crystal was annealed for 240 h, corresponding to an almost complete replacement of the extra-framework O^{2-} ions with electrons.

Electrical conductivity behavior changes from semiconductor type to degenerated one with increasing the electron concentration. When the electron concentration was on the order of $10^{19}\,cm^{-3}$, the temperature dependence of the Ca-reduced C12A7 is nearly the same as that in the UV-illuminated C12A7:H^- (Fig. 11), suggesting that inter-cage hopping of electrons are responsible for the electron transport in the Ca-reduced C12A7 as well. A dramatic increase in the conductivity at high electron concentrations indicates that the electrons become more delocalized. Even higher electron concentration may cause metallic conduction in C12A7.[47]

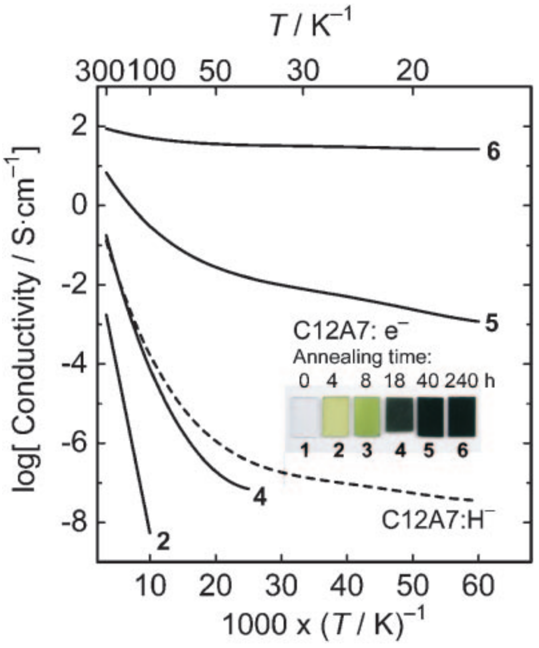

Fig. 11. The Arrehnius plot of electrical conductivity in the Ca-reduced C12A7 single crystals.[46] Inset is a photograph of a series of processed single crystals. The solid lines show the conductivity of each sample. Dashed line is that of an UV-illuminated C12A7:H^-.[35]

As expected for traditional organic electrides, the C12A7 electride was also found to have a high potential for the cold-cathode electron emission in a vacuum.[48] Furthermore, a high-intensity thermal field electron emission was observed by heating at 600–900 °C,[49] demonstrating an unprecedented stability as an electride. In addition, unique fabrication routes are available in the case of C12A7 electrides, such as a solidification of C12A7 melt in carbon crucibles[50] and a hot ion implantation of inert gas ions into films.[51] These processes have not been possible for other electrides.

6. Origin of Active Anion Formations

In this section, aspects of stable formation of active anion species in the cages will be examined based on electronic structure, thermodynamics, and structural features of the cage.

6.1 Extra-Framework O^{2-} Ion. We first analyze the extra-framework O^{2-} ion, whose selective replacement is likely a key step in the formation of the active anions in this system. Figure 12a is an energy diagram of the C12A7 framework and 2p states of extra-framework F^-, OH^-, and O^{2-} ions calculated by the first-principle calculation. The 2p states of framework O^{2-} ion principally form the valence band, while 2p states of the extra-framework O^{2-} ion are split from valence band, so that the highest occupied molecular orbital (HOMO) is located in the band gap ≈ 1.8 eV above VBM. As the extra-framework species is replaced by more stable anions, the 2p level tends to be lowered; OH^- level is just above VBM and that of F^- locates inside the valence band. These levels are directly verified by the optical absorption

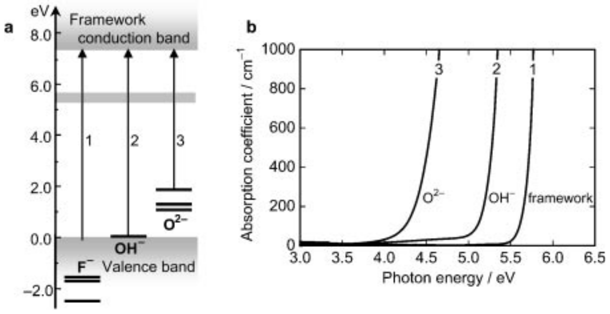

Fig. 12. Lift of 2p levels of extra-framework O^{2-} ion with respect to the framework O^{2-} ions. (a) Schematic energy level diagram obtained from the first-principle theoretical calculation. Arrows with numbers indicate transitions responsible for the corresponding to the optical absorptions. (b) The experimental optical absorption spectra of C12A7 crystals: 1, doped with F^- ions by an annealing with CaF_2; 2, doped with OH^- ions by annealing in wet atmosphere; 3, with near-stoichiometric composition by annealing in an inert gas atmosphere.[52]

spectroscopy. Figure 12b shows absorption spectra of C12A7 crystals, whose cages are almost completely occupied by F^-, OH^-, or O^{2-} ions. The absorption edge energy increases in the order of O^{2-}, OH^-, and F^-. Those of C12A7 with O^{2-} and OH^- are attributable to transitions from 2p level to CB, while that of the F^--substituted C12A7 is due to the transition from VBM to FCBM. The lowest absorption edge is observed in the O^{2-} incorporating sample, demonstrating that HOMO of the extra-framework O^{2-} ion is the highest compared to these three anions.[52]

The above results indicate that environment of O^{2-} ion in the cage is significantly differs from that in the framework presumably due to a difference in the Madelung potential between the cage site and the framework O^{2-} ion site: only 1/3 of an elemental charge is allocated to each cage, and the free space of the cage is approximately 40% larger than that of the O^{2-} ion site in conventional metal oxides. Thus, the extra-framework O^{2-} ion is less stable and more basic, facilitating their selective substitution for the active anions, electron donation to another species like the process in Eq. 2, and the abstraction of hydrogen as in Eq. 4. Such a low crystal field inside the cage is most likely the principal reason for the stable active anion formation in C12A7.

6.2 Thermodynamic Assessment of Extra-Framework Species. Extra-framework species examined in this study are summarized in the phase diagram in Fig. 13a. So far, only compositions on the tie line between O^{2-} and $2OH^-$ were recognized in C12A7. We expanded the available compositions considerably. It is noted Ca–O–H compound system may show a similar diagram shown in Fig. 13b, such that $(Ca_{12}Al_{14}O_{32})^{2+}\cdot O^{2-}$ corresponds to CaO and $(Ca_{12}Al_{14}O_{32})^{2+}\cdot 2OH^-$ to $Ca(OH)_2$. Comparison between the two systems is helpful to quantitatively clarify the stable formation of extra-framework species in C12A7. Table 1 lists enthalpy change of several reactions concerning the extra-framework species, and those of corresponding reactions in the Ca–O–H system. Representative ΔH values are shown by the bar heights in Fig. 13, where the O^{2-} composition is taken as the origin of the ΔH value, and O_2 and H_2O gases, which are present stably in ambient air, are taken as standards. Comparison of the formation enthalpies clearly demonstrates that formation of anions in the C12A7 system is much stable than those in the Ca–O–H system, substantiating that C12A7 can easily form the active anions that hardly occur in conventional metal-oxides.

6.2.1 Stability of Each Species: The most stable extra-framework species in ambient atmosphere is OH^- ion. Usually the conventional C12A7 contains OH^- ions in the cages. This stable form of C12A7 has likely masked the true potential of this material for long time. Suppressing the formation of OH^- enables the formation of active anions.

Reaction 3 in Table 1 (Eq. 2 in the text) describes the formation of oxygen radicals by the incorporation of excess oxygen into C12A7. The negative enthalpy change indicates that these monovalent anions are "stable" in C12A7, despite the fact that oxygen in metal-oxides usually takes divalent state. Such an exceptional situation in the cage is analogous to gas phase, judging from the negative enthalpy change for the corresponding reaction in gas phase (Reaction 2), although ΔH in the gas phase exhibits much larger negative value (-9.2 eV)[25] due to the large second electron affinity of oxygen ($+8.7$ eV). While in metal oxides, the O^{2-} ion is fairly stable due to the

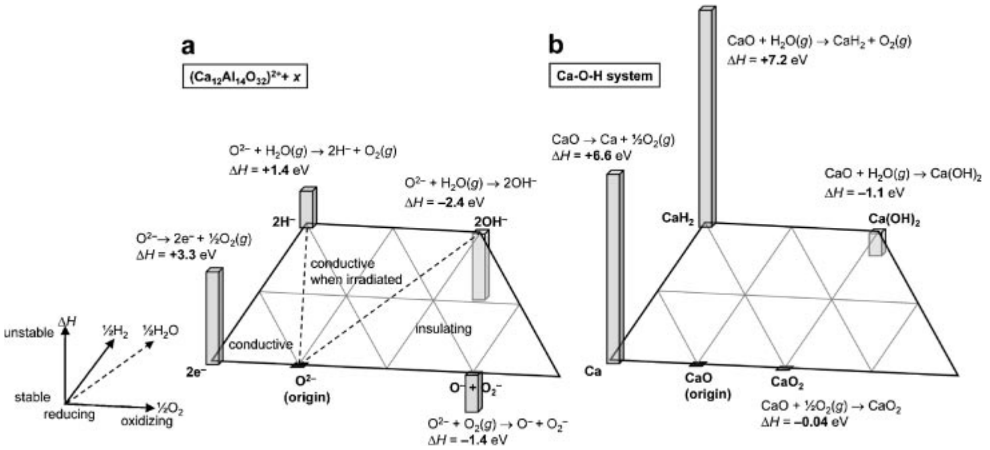

Fig. 13. Phase diagram of extra-framework species in C12A7 and Ca–H–O compound system. Formation enthalpy of each species and phases are shown by bar heights.

Table 1. Enthalpy Changes in Reactions: in Gas Phase (Nos. 1 and 2), Concerning the Extra-Framework Species in C12A7 Evaluated Experimentally (Nos. 3–6), Calculated from Nos. 1–6 (Nos. 7–11), and in the Ca–O–H Compound System (Nos. 12–15)

	System	Process[a)]	ΔH/eV	Reference[b)]
(1)	Gas phase	$2H_2(g) + O_2(g) \rightarrow 2H_2O(g)$	−5.2	54
(2)	Gas phase	$O^{2-}(g) + O_2(g) \rightarrow O^-(g) + O_2{}^-(g)$	−9.2	25
(3)	C12A7	$O^{2-}(c) + O_2(g) \rightarrow O^-(c) + O_2{}^-(c)$	−1.4	25
(4)	C12A7	$O^{2-}(c) + H_2O(g) \rightarrow 2OH^-(c)$	−2.4	20
(5)	C12A7	$2e^-(c) + 1/2O_2(g) \rightarrow O^{2-}(c)$	−3.3	53
(6)	C12A7	$2e^-(c) + OH^-(c) \rightarrow H^-(c) + O^{2-}(c)$	−1.4	42
(7)	C12A7	$O^{2-}(c) + H_2O(g) \rightarrow 2H^-(c) + O_2(g)$	+1.4	(4) − 2[(5) − (6)]
(8)	C12A7	$O^{2-}(c) + 2H_2(g) \rightarrow 2H^-(c) + H_2O(g)$	−3.8	(1) + (7)
(9)	C12A7	$2e^-(c) + H_2(g) \rightarrow 2H^-(c)$	−4.5	(5) + 1/2[(7) + (8)]
(10)	C12A7	$H^-(c) + 1/2O^-(c) + 1/2O_2{}^-(c) \rightarrow OH^-(c) + 1/2O^{2-}(c)$	−1.2	−1/2(3) + (5) − (6)
(11)	C12A7	$e^-(c) + 1/2O^-(c) + 1/2O_2{}^-(c) \rightarrow 2O^{2-}(c)$	−1.0	−1/2(3) + 1/2(5)
(12)	Ca–O–H compounds	$CaO(s) + 1/2O_2(g) \rightarrow CaO_2(s)$	−0.04	54
(13)	Ca–O–H compounds	$CaO(s) + H_2O(g) \rightarrow Ca(OH)_2(s)$	−1.1	54
(14)	Ca–O–H compounds	$Ca(s) + 1/2O_2(g) \rightarrow CaO(s)$	−6.6	54
(15)	Ca–O–H compounds	$CaO(s) + H_2O(g) \rightarrow CaH_2(s) + O_2(g)$	+7.2	54

a) Gas phase and crystalline solid phase are indicated by (g) and (s), respectively. Anions formed in the cages of C12A7 are indicated by (c). Empty cages are omitted. b) Parentheses indicate the reaction number in this table.

Mardelung potential of the crystal. Thus, observed negative value in the Reaction 3 likely ascribed to the instability of the extra-framework O^{2-} ion under a weak crystal potential in the cage.

The value of ΔH for H^- ion formation in the cage, which has not been directly measured experimentally, is calculated from reactions 1 and 4–6. The ΔH value in Reaction 7 is positive, indicating H^- ion formation is quite difficult in ambient air. However, since Reaction 8 has a negative ΔH value, H^- ions are easily formed by employing a hydrogen-reduction process. Moreover, it is expected from Reaction 9 that the electride easily reacts with hydrogen gas to form H^- ions in the cage, suggesting that both hydrogen and oxygen must be eliminated from the reaction atmosphere to maximize the electron concentration in the electride.

The presence of H^- ion in metal oxides has been controversial recently. One reason is the lack of clear experimental evidence for its existence; detection methods and limitation of kinds of materials so far investigated. The other and probably the dominant reason is that the H^- ion in metal-oxides may be far more stable than that predicted from thermodynamic stability of metal-hydride crystals.[55] Because the thermodynamic stability of H^- in C12A7 is quite reasonable, this reduced hydrogen species should shift focus towards other metal oxides in the future.

6.2.2 Coexisting Extra-Framework Species and Electrical Conductivity: Here, we consider that extra-framework species that coexist at an arbitrary O–H composition on the basis of the enthalpy change without accounting for the entropy contributions. That is, an evaluation of the equilibrium states at 0 K. Nevertheless, this evaluation is a reasonable approximation for predicting room temperature states. The O–H composition field shown in Fig. 13a is divided into three regions according to the kind of coexisting extra-framework species. In the "insulating" region, O^{2-}, OH^-, and oxygen radical anions can coexist with each other. As evidenced by the negative enthalpy changes in Reactions 10 and 11 in Table 1, H^- ions and electrons virtually cannot coexist with oxygen radicals in this region, because they are converted to OH^- and/or O^{2-} ions under the equilibrium. Thus, C12A7 in this region is electrically insulating. The absence of a persistent electron in this region is consistent with the fact that the O^- emission to vacuum accompanies with the emission of few electrons. On the other hand, in the region partitioned by $2O^{2-}$, $2OH^-$, and $2H^-$, Reactions 4 and 9 demonstrate that electrons and oxygen radicals are not formed under the equilibrium, and thereby C12A7 becomes diamagnetic insulator. It is interesting that both anionic (H^-) and cationic (H^+ in OH^-) hydrogen can coexist with each other. Their coexistence is not exceptional but predicted to be general in many compound semiconductor and metal-oxide systems with "negative U" character.[56,57] If extra-framework H^- and O^{2-} ions are present, irradiation or high-temperature equilibrium generates electrons, leading to a metastable conductive state. Finally in the "conductive" region, C12A7 is intrinsically conductive due to the presence of thermodynamically stable electrons, which can coexist only with H^- and O^{2-} ions.

6.3 Inner Cage as a Surface of Metal Oxide. Anion species treated in this study are found typically in ionic crystals with most electropositive elements: alkali or alkaline-earth metal oxides. These metal elements form the stable binary compounds with active anions,[58] for example, CaH_2 for H^- ion, and NaO_2 for $O_2{}^-$ ion. They are useful as chemical agents, for example, CaH_2 as a reducing agent and NaO_2 as the chemical oxygen generator. Active anions are also formed stably at the anion vacancies in ionic crystals composed of these metal cations. The crystals form various color centers: OH^-, $O_2{}^-$, and O^- centers,[59] and U center[60] (H^- ion trapped at the anion vacancy in alkali halides) as well as F and F^+ centers. Thus, cations of alkali or alkaline-earth elements has an high affinity for these active anions. Unfortunately, most of these binary compounds or host ionic crystals are not suitable for practical uses as functional "materials," because they are unstable or deliquescent in ambient atmosphere.

One exceptional case is a fine-grained MgO used as catalysts where various active anions are formed on the surface and responsible for the surface reactions. Considering similarities and differences between inner cage of C12A7 and surface of MgO will be helpful for elucidating the origin of the active anion derived functionalities of C12A7.

Oxygen deficient sites on the surface of dehydrated MgO can trap one or two electrons. The most stable form is the F_S center that traps two electrons in the oxygen deficient sites, where the suffix S denotes the surface. Electron donation from the F_S center cause a heterolytical dissociation to form a pair of H^- ion and OH^- groups when the surface is exposed to H_2 gas, while $O_2{}^-$ ion is formed on Mg cation site when exposed to O_2 gas.[61] The one-electron paramagnetic state is also stabilized when combined with OH^- groups formed nearby. This color center, termed $F_S{}^+$(H) center, is created by exposure to H_2 gas and subsequent UV-irradiation. The photolysis of the surface H^- ion is responsible for the creation of this center. This process is quite similar to the UV-induced F^+-like center formation in C12A7. It is also known that a further exposure of N_2O to the $F_S{}^+$(H) center results in the formation of surface O^- defect.[62] These monovalent species tend to prefer lower coordination sites: both H^- and $F_S{}^+$(H) centers prefer corner anion vacancy sites[63] most likely due to a small Pauli repulsion with coordinating ions[64] and O^- defects prefers vertex anion sites attributable to lower crystalline potential.[65] It is known that an adsorption of $O_2{}^-$ ion on Mg^{2+} ion is enhanced as coordination number becomes smaller due to stronger local crystal field.[66] Unlike C12A7, these reactions on MgO surface are not reversible, and they occur immediately even below room temperature.

The behavior of the active anions formed on MgO surface suggests that the surface, especially lower coordination sites, provides a preferable environment to stabilize the active anions in metal-oxide systems. Similar situation is also found in the inner surface of the cage in C12A7. As found in Fig 1b, the large inner space of the cage suggests that the cage wall is regarded as a kind of surface. Moreover, the cage wall provides an effectively lower coordination site for anions suitable for trapping the monovalent anions. The number of Ca ions in each cage wall is six, which is equal to the coordination number of an anion vacancy in CaO crystal. However there are two types of Ca ion, when viewed from the cage center, although the Ca atoms occupy only one crystallographic site in the C12A7 crystal. Two Ca ions occupy the opposite side on the S_4 axis (See Fig. 1). These Ca ions have nearly planar 4-coordination (there are additional 2-coorination outside of the relevant cage), and hence, are exposed to inside the cage like the Ca ions on the CaO surface, while the other four Ca ions are effectively screened by the framework O^{2-} ions.[43] The two Ca ions on the S_4 axis are responsible for trapping the active anions. Indeed our EPR study on $O_2{}^-$ ion in the cage at low temperature showed that the $O_2{}^-$ ion is bound to one of the Ca ions on the S_4 axis.[21] Furthermore, as demonstrated by the theoretical calculation, displacement of these Ca ions in H^- ions or electron-accommodating cages contributes largely to the stabilization of these active anions. In contrast, extra-framework O^{2-} ion provides highly basic site for trapping the H^+ ion as demonstrated in the previous subsection. Accordingly, C12A7 may be regarded as a material where active sites associated with a CaO surface are incorporated in an alumina framework.

The size of cage is also responsible for the anion manipulation ability of C12A7. Unlike the MgO surface, the inner cage space of zeolites and other mesoporous materials, the inner cage of C12A7 is not directly accessible by outer chemical species at room temperature due to the small openings. Thus, the formation of active anions in the cages requires temperatures high enough for the bulk diffusion of relevant species, while these active anions are stably preserved around room temperature even exposed to the ambient atmosphere. However, each cage is not isolated unlike the anion defects in alkali halides; linkage of the cages is responsible for the electron transportation. Such a unique encapsulated environment also makes internal reactions that are similar to MgO surface reactions, e.g. the UV-induced electron generation at room temperature, possible.

7. Concluding Remarks

Novel characteristics were found in C12A7 by the incorporation of active anion species into cages that are embedded in the positively charged lattice framework. The characteristics include formation of abundant oxygen radicals, efficient field-extraction of O^- ions to vacuum, light- or electron-beam-induced insulator–conductor conversion, formation of stable electride, and electron emission from the electride. The cage provides the environment preferable to the stable formation of active anions.

This study suggests that the use of natural nanostructures constructed by main-group light elements, like the cage of C12A7, is beneficial for the formation of active anions. Contrary to artificial nanostructures, natural nanostructure is formed as a result of its thermodynamic stability. Furthermore, oxides of the main-group light metals are highly resistant to reduction. Such stabilities are suitable for the formation of H^- ions or electrons. The main-group light elements also include cationic elements that form a TO_4 tetrahedron, such as B, Al, Si, P, etc., of which the vertex linkages in the crystal allow the construction of a nanostructure suitable for the incorporation of extrinsic species, as has been typically observed in zeolites. In addition, the alkaline or alkaline-earth metals have a higher affinity for the active anions. Accordingly, nanostructures constructed by a combination of TO_4 elements and alkali or alkaline-earth metals may fulfill the conditions necessary for the formation of stable active anions formation. However, these characteristics are not special to the C12A7, but are general to many natural minerals. Thus, reexamination of nanostructures observed in natural minerals may be a promising strategy for discovering novel functionalities originating from active anions.

We thank Drs. Satoru Matsuishi, Masashi Miyakawa, Sung-Wng Kim, Yoshikake Toda, and Toshio Kamiya of Tokyo Institute of Technology, Peter V. Sushko and Alexander L. Shluger of University College London, U.K., Masayoshi Sadakata of The University of Tokyo (now at Kogakuin

University) and Isao Tanaka of Yamanashi University for collaborative works, and SM and PVS for providing materials for figures.

This work is supported by the Grant-in-Aid for Creative Scientific Research (No. 16GS0205) from the JSPS, the Grant-in-Aid for Young Scientists B (No. 17750193) from the MEXT, and by a Grant-in-Aid for Industrial Technology Research (No. 05A25513a) from the NEDO. A part of the research was performed within the framework of the ERATO program (Hosono Transparent Electro-Active Materials Project) sponsored by JST.

References

1 *Calcium Aluminate Cements 2001*, ed. by R. J. Mangabhai, F. P. Glasser, IOM Communications, London, **2001**.

2 H. B. Bartl, T. Scheller, *Neues Jahrb. Mineral., Monatsh.* **1970**, *35*, 547.

3 M. Lacerda, J. T. S. Irvine, F. P. Glasser, A. R. West, *Nature* **1988**, *332*, 525.

4 R. W. Nurse, J. H. Welch, A. Majumdar, *Trans. Br. Ceram. Soc.* **1965**, *64*, 323.

5 J. Jeevaratnam, F. P. Glasser, L. S. D. Glasser, *J. Am. Ceram. Soc.* **1964**, *47*, 105.

6 K. Hayashi, M. Hirano, H. Hosono, *J. Mater. Res.* **2002**, *17*, 1244.

7 B. Hallstedl, *J. Am. Ceram. Soc.* **1990**, *73*, 15.

8 W. R. Whatmore, C. O'Hare, B. Cockayne, *Mater. Res. Bull.* **1979**, *14*, 967.

9 S. Watauchi, I. Tanaka, K. Hayashi, M. Hirano, H. Hosono, *J. Cryst. Growth* **2002**, *237–239*, 801.

10 H. Hosono, K. Yamazaki, Y. Abe, *J. Am. Ceram. Soc.* **1987**, *70*, 867.

11 K. Kurashige, Y. Toda, S. Matsuishi, K. Hayashi, M. Hirano, H. Hosono, *Cryst. Growth Des.* **2006**, *6*, 1602.

12 Y. Toda, M. Miyakawa, K. Hayashi, T. Kamiya, M. Hirano, H. Hosono, *Thin Solid Films* **2003**, *445*, 309.

13 M. Miyakawa, K. Hayashi, M. Hirano, Y. Toda, T. Kamiya, H. Hosono, *Adv. Mater.* **2003**, *15*, 1100.

14 W. Li, B. S. Mitchell, *J. Non-Cryst. Solids* **1999**, *255*, 199.

15 M. Che, A. J. Tench, *Adv. Catal.* **1983**, *32*, 1.

16 C. Naccache, *Chem. Phys. Lett.* **1971**, *11*, 323.

17 H. Hosono, Y. Abe, *Inorg. Chem.* **1987**, *26*, 1192.

18 K. Hayashi, M. Hirano, S. Matsuishi, H. Hosono, *J. Am. Chem. Soc.* **2002**, *124*, 738.

19 K. Hayashi, S. Matsuishi, N. Ueda, M. Hirano, H. Hosono, *Chem. Mater.* **2003**, *15*, 1851.

20 K. Hayashi, M. Hirano, H. Hosono, *J. Phys. Chem. B* **2005**, *109*, 11900.

21 K. Hayashi, S. Matsuishi, M. Hirano, H. Hosono, *J. Phys. Chem. B* **2004**, *108*, 8920.

22 S. Yang, J. N. Kondo, K. Hayashi, M. Hirano, K. Domen, H. Hosono, *Chem. Mater.* **2004**, *16*, 104.

23 K. Hayashi, M. Hirano, H. Hosono, *Chem. Lett.* **2005**, *34*, 586.

24 P. V. Sushko, A. L. Shluger, K. Hayashi, M. Hirano, H. Hosono, *Phys. Rev. B* **2006**, *73*, 014101.

25 K. Hayashi, S. Matsuishi, M. Hirano, H. Hosono, *J. Phys. Chem. B* **2004**, *108*, 8920.

26 K. Hayashi, N. Ueda, M. Hirano, H. Hosono, *Solid State Ionics* **2004**, *173*, 89.

27 H. Tsuji, J. Ishikawa, T. Tomita, Y. Gotoh, *Rev. Sci. Instrum.* **1996**, *67*, 1012.

28 Y. Torimoto, A. Harano, T. Suda, M. Sadakata, *Jpn. J. Appl. Phys.* **1997**, *36*, L238.

29 M. Nishioka, Y. Torimoto, H. Kashiwagi, Q. Li, M. Sadakata, *J. Catal.* **2003**, *215*, 1.

30 Q. Li, K. Hayashi, M. Nishioka, H. Kashiwagi, M. Hirano, Y. Torimoto, H. Hosono, M. Sadakata, *Appl. Phys. Lett.* **2002**, *80*, 4259.

31 K. Hayashi, M. Hirano, Q. Li, M. Nishioka, M. Sadakata, Y. Torimoto, S. Matsuishi, H. Hosono, *Electorochem. Solid State Lett.* **2002**, *5*, J13.

32 Q. Li, K. Hayashi, M. Nishioka, H. Kashiwagi, M. Hirano, Y. Torimoto, H. Hosono, M. Sadakata, *Jpn. J. Appl. Phys.* **2002**, *41*, L530.

33 Q. Li, H. Hosono, M. Hirano, K. Hayashi, M. Nishioka, H. Kashiwagi, Y. Torimoto, M. Sadakata, *Surf. Sci.* **2003**, *527*, 100.

34 N. Ando, K. Hayashi, T. Kamiya, H. Hosono, Abstracts of Annual Meeting of The Ceramic Society of Japan, **2006**, p. 74.

35 K. Hayashi, S. Matsuishi, T. Kamiya, M. Hirano, H. Hosono, *Nature* **2002**, *419*, 462.

36 K. Hayashi, Y. Toda, T. Kamiya, M. Hirano, M. Yamanaka, I. Tanaka, T. Yamamoto, H. Hosono, *Appl. Phys. Lett.* **2005**, *86*, 22109.

37 P. V. Sushko, A. L. Shluger, K. Hayashi, M. Hirano, H. Hosono, *Phys. Rev. Lett.* **2003**, *91*, 126401.

38 P. V. Sushko, A. L. Shluger, K. Hayashi, M. Hirano, H. Hosono, *Thin Solid Films* **2003**, *445*, 161.

39 P. V. Sushko, A. L. Shluger, K. Hayashi, M. Hirano, H. Hosono, *Mater. Sci. Eng., C* **2005**, *25*, 722.

40 P. V. Sushko, A. L. Shluger, K. Hayashi, M. Hirano, H. Hosono, *Appl. Phys. Lett.* **2005**, *86*, 92101.

41 S. Matsuishi, K. Hayashi, M. Hirano, H. Hosono, *J. Am. Chem. Soc.* **2005**, *127*, 12454.

42 P. V. Sushko, A. L. Shluger, K. Hayashi, M. Hirano, H. Hosono, *Phys. Rev. B* **2006**, *73*, 045120.

43 K. Hayashi, P. V. Sushko, A. L. Shluger, M. Hirano, H. Hosono, *J. Phys. Chem. B* **2005**, *109*, 23836.

44 J. L. Dye, *Inorg. Chem.* **1997**, *36*, 3816.

45 A. S. Ichimura, J. L. Dye, M. A. Camblor, L. A. Villaescusa, *J. Am. Chem. Soc.* **2002**, *124*, 1170.

46 S. Matsuishi, Y. Toda, M. Miyakawa, K. Hayashi, M. Hirano, I. Tanaka, H. Hosono, *Science* **2003**, *301*, 626.

47 S.-W. Kim, S. Matsuishi, T. Nomura, Y. Kubota, M. Takata, K. Hayashi, T. Kamiya, M. Hirano, H. Hosono, *Nano Lett.* **2007**, in press.

48 Y. Toda, S. Matsuishi, K. Hayashi, K. Ueda, T. Kamiya, M. Hirano, H. Hosono, *Adv. Mater.* **2004**, *16*, 685.

49 Y. Toda, S.-W. Kim, K. Hayashi, M. Hirano, T. Kamiya, H. Hosono, T. Haraguchi, H. Yasuda, *Appl. Phys. Lett.* **2005**, *87*, 254103.

50 S.-W. Kim, M. Miyakawa, K. Hayashi, T. Sakai, M. Hirano, H. Hosono, *J. Am. Chem. Soc.* **2005**, *127*, 1370.

51 M. Miyakawa, Y. Toda, K. Hayashi, T. Kamiya, M. Hirano, N. Matsunami, H. Hosono, *J. Appl. Phys.* **2005**, *97*, 23510.

52 K. Hayashi, P. V. Sushko, D. Muñoz Ramo, A. L. Shluger, S. Watauchi, I. Tanaka, S. Matsuishi, M. Hirano, H. Hosono, *J. Phys. Chem. B* **2007**, *111*, 1946.

53 O. Trofymluk, Y. Toda, H. Hosono, A. Navrotsky, *Chem. Mater.* **2005**, *17*, 5574.

54 Calculated using MALT program, Kagaku Gijutsu-Sha, Japan: H. Yokokawa, S. Yamauchi, T. Matsumoto, *CALPHAD:*

Comput. Coupling Phase Diagrams Thermochem. **2002**, *26*, 155.

55 T. Norby, M. Widerøe, R. Glöckner, Y. Larring, *Dalton Trans.* **2004**, 3012.

56 C. G. Van de Walle, J. Neugebauer, *Nature* **2003**, *423*, 626.

57 S. F. J. Cox, J. L. Gavartin, J. S. Lord, S. P. Cottrell, J. M. Gil, H. V. Alberto, J. Piroto Duarte, R. C. Vilão, N. Ayres de Campos, D. J. Keeble, E. A. Davis, M. Charlton, D. P. van der Werf, *J. Phys.: Condens. Matter* **2006**, *18*, 1079.

58 F. A. Cotton, G. Wilkinson, *Advanced Inorganic Chemistry*, Wiley, New York, **1980**, Chap. 6.

59 F. Fischer, H. Gründig, R. Hilsch, *Z. Phys.* **1966**, *189*, 79.

60 H. W. Etzel, D. A. Patterson, *Phys. Rev.* **1958**, *112*, 1112.

61 D. M. Murphy, R. D. Farley, I. J. Purnell, C. C. Rowlands, A. R. Yacob, M. Cristina, E. Giamello, *J. Phys. Chem. B* **1999**, *103*, 1944.

62 M. Sterrer, O. Diwald, E. Knözinger, *J. Phys. Chem. B* **2000**, *104*, 3601.

63 M. C. Paganini, M. Chiesa, E. Giamello, S. Coluccia, G. Martra, D. M. Murphy, G. Pacchioni, *Surf. Sci.* **1999**, *421*, 246.

64 G. Pacchioni, P. Pescarmona, *Surf. Sci.* **1998**, *412–413*, 657.

65 P. V. Sushko, A. L. Shluger, C. R. A. Catlow, *Surf. Sci.* **2000**, *450*, 153.

66 G. Pacchioni, A. M. Ferrari, E. Giamello, *Chem. Phys. Lett.* **1996**, *255*, 58.

Award recipient

Katsuro Hayashi was born in Toyama prefecture in 1972. He received a B.E. degree in 1995 and a Ph.D. degree in 2000 from The University of Tokyo. He worked as a researcher at Hosono Transparent Electro-Active Materials (TEAM) project, ERATO, funded by Japan Science and Technology Agency (JST) from 2000 to 2004. He joined the Frontier Collaborative Research Center, Tokyo Institute of Technology as a Research Associate in 2004, and was appointed to an Associate Professor of Secure Materials Center, Materials and Structures Laboratory in 2006. His awards include Japan Institute of Metals Award for Young Scientist in 2003, and the Chemical Society of Japan Award for Young Chemists in 2006. His research interests include transport phenomena, physics and chemistry of defects in oxides, and their applications.

Masahiro Hirano received a B.E. degree in 1966, and a Ph.D. degree in 1971 from The University of Tokyo. He joined Electrotechnical Laboratory of MITI in 1971. He was with Optoelectronic Industry and Technology Association from 1981 to 1984 and Optoelectronic Joint Research Laboratory from 1984 to 1987. He worked for Asahi Glass Company from 1988 to 1999. He has been with TEAM project in the framework of ERATO (1999–2004) and ERATO-SORST (2004–) as a research manager. He is also a Professor of Frontier Collaborative Research Center, Tokyo Institute of Technology. His research interests cover magnetic, opto-electronic, oxides and nanotech materials.

Hideo Hosono received a B.E. degree in 1977 and a Ph.D. degree in 1982 from Tokyo Metropolitan University. He became a Professor of Materials and Structures Laboratory, Tokyo Institute of Technology in 1999 after being an Associate Professor of Nagoya Institute of Technology and Institute of Molecular Science. He was appointed to a Professor of Frontier Collaborative Research Center in 2004. He was the leader of the ERATO-TEAM project (1999–2004), and is now leading the ERATO-SORST project (2004–) and the 21st Century COE program (2002–). His current research focuses are novel function exploration in wide-gap crystalline and amorphous oxides.